The Astrophysical Journal, 950:190 (11pp), 2023 June 20 https://doi.org/10.3847/1538-4357/acd004

High-energy Neutrino Emission Associated with Gravitational-wave Signals: Effects of Cocoon Photons and Constraints on Late-time Emission

Riki Matsui[1], Shigeo S. Kimura[1,2], Kenji Toma[1,2], and Kohta Murase[3,4,5]
[1] Astronomical Institute, Graduate School of Science, Tohoku University, Sendai 980-8578, Japan; riki.matsui@astr.tohoku.ac.jp
[2] Frontier Research Institute for Interdisciplinary Sciences, Tohoku University, Sendai 980-8578, Japan
[3] Department of Physics; Department of Astronomy and Astrophysics; Center for Multimessenger Astrophysics, Institute for Gravitation and the Cosmos, The Pennsylvania State University, University Park, PA 16802, USA
[4] School of Natural Sciences, Institute for Advanced Study, USA
[5] Center for Gravitational Physics and Quantum Information, Yukawa Institute for Theoretical Physics, Kyoto University, Kyoto, Kyoto 606-8502, Japan
Received 2023 February 9; revised 2023 April 13; accepted 2023 April 23; published 2023 June 26

Abstract

We investigate prospects for the detection of high-energy neutrinos produced in the prolonged jets of short gamma-ray bursts (sGRBs). The X-ray light curves of sGRBs show extended emission components lasting for 100–1000 s, which are considered to be produced by prolonged engine activity. Jets produced by such activity should interact with photons in the cocoon formed by the propagation of the jet inside the ejecta of neutron star mergers. We calculate neutrino emission from jets produced by prolonged engine activity, taking account of the interaction between photons provided from the cocoon and cosmic rays accelerated in the jets. We find that IceCube-Gen2, a future neutrino telescope, with second-generation gravitational-wave detectors will probably be able to observe neutrino signals associated with gravitational waves with around 10 years of operation, regardless of the assumed value of the Lorentz factor of the jets. Neutrino observations may enable us to constrain the dissipation region of the jets. We apply this model to GRB 211211A, a peculiar long GRB whose origin may be a binary neutron star merger. Our model predicts that IceCube is unlikely to detect any associated neutrinos, but a few similar events will be able to put a meaningful constraint on the physical quantities of the prolonged engine activities.

Unified Astronomy Thesaurus concepts: Neutrino astronomy (1100); Particle astrophysics (96); Gamma-ray bursts (629); Gravitational wave astronomy (675); Neutron stars (1108)

1. Introduction

Binary neutron star (BNS) mergers are one of the most important targets of gravitational-wave (GW) observations and electromagnetic (EM) follow-up observations. Immediately after the first BNS merger event, GW170817, a short gamma-ray burst (sGRB) was identified as an EM counterpart (Abbott et al. 2017a, 2017b, 2017c). Radio observations show the superluminal motion (Mooley et al. 2018b), and radio to X-ray counterparts are well modeled by off-axis afterglow emission from a structured relativistic jet (Mooley et al. 2018a, 2018b; Troja et al. 2018; Ghirlanda et al. 2019; Lamb et al. 2019). These studies support BNS mergers as the progenitor of sGRBs.

The formation mechanism and dissipation process of sGRB jets, however, are still unknown, despite a lot of theoretical and observational studies (Berger 2014). The standard afterglow scenario cannot explain typical X-ray light curves of sGRBs, where we see some excesses on a timescale of 10^2–10^5 s after the prompt emission (Norris & Bonnell 2006; Sakamoto et al. 2011; Kagawa et al. 2015; Kaneko et al. 2015, 2019). These emission components, called extended and plateau emissions, are considered evidence of prolonged central engine activity (Ioka et al. 2005; Perna et al. 2006; Metzger et al. 2008; Rowlinson et al. 2013; Gompertz et al. 2014; Kisaka & Ioka 2015; Kisaka et al. 2017). Current observations provide little constraint on the physical quantities of late-time emission components, including composition, Lorentz factor, and dissipation radius.

High-energy neutrinos are considered a powerful probe to investigate the physical quantities of gamma-ray bursts (GRBs; Waxman & Bahcall 1997; Guetta et al. 2004; Murase & Nagataki 2006a; He et al. 2012; Hümmer et al. 2012; Li 2012; Kimura et al. 2017). When jets dissipate their kinetic energy, electrons are nonthermally accelerated by some process, such as first-order Fermi acceleration, and produce gamma rays observed as GRBs. If protons of PeV to EeV energies are accelerated at the same time, photohadronic interactions can produce neutrinos with energies above 1 PeV (Kimura 2022). Observing such neutrinos in addition to EM wave signals enables us to investigate the physical mechanism of GRBs.

The neutrino observatory, IceCube, has been detecting high-energy neutrinos from astrophysical objects and trying to determine their source for more than 10 years (Aartsen et al. 2013, 2020; IceCube Collaboration et al. 2021). Despite the expectation of neutrino emission from GRBs, GRB analyses by IceCube Collaboration revealed no significant spatial and temporal associations between cosmic neutrino events and GRBs (Abbasi et al. 2010, 2011; IceCube Collaboration et al. 2012; Aartsen et al. 2015, 2016, 2017a; Abbasi et al. 2022), which puts an upper limit on neutrino emission from GRBs. Future cosmic high-energy neutrino detectors, such as IceCube-Gen2 (Aartsen et al. 2021), KM3Net/ARCA (Aiello et al. 2019), baikal-GVD (Avrorin et al. 2014), P-One (Agostini et al. 2020), and TRIDENT (Ye et al. 2022), will significantly increase the detection rate of cosmic neutrinos. We should estimate neutrino emissions from various environments to efficiently interpret the data.

When we consider prolonged engine activity, the matter ejected by the BNS merger can play an important role in the high-energy component of late-time emissions. A BNS merger ejects outflowing material (ejecta), as confirmed by optical/infrared counterparts to GW170817 (Kasen et al. 2017; Kasliwal et al. 2017; Murguia-Berthier et al. 2017; Shibata et al. 2017; Tanaka et al. 2017). The sGRB jet can interact with the ejecta if the jet formation is delayed from the merger, which leads to the formation of a cocoon (Bromberg et al. 2011; Hamidani et al. 2020; Hamidani & Ioka 2021). The cocoon can introduce photons into the dissipation region of prolonged jets. Leptonic emission considering the external photons from the cocoon has been discussed (Toma et al. 2009; Kimura et al. 2019), but hadronic emissions with the cocoon photons are not considered in detail.

In this study, we calculate the production of high-energy neutrinos through the interaction of photons with cosmic rays accelerated inside the jet, taking into account the cocoon photons entering the prolonged jet. We also calculate the possibility of detecting neutrinos at the late time of sGRBs associated with GWs, based on the sensitivities of IceCube and IceCube-Gen2 (IceCube Collaboration et al. 2021). The calculation shows that after $\sim$10 yr of observation by IceCube-Gen2, it is highly probable to observe one or more neutrinos in this scenario, or we can constrain the parameters with a 2σ or 3σ confidence level. This result is almost independent of the Lorentz factor of jets, which may enable us to put a stronger constraint on the dissipation radius than that without cocoon photons. We describe our model and show the neutrino spectra in Section 2. In Section 3, we discuss the probability of neutrino detection with current and future detectors. In Section 4, we apply our model to GRB 211211A, a peculiar long GRB whose origin may be a BNS merger. Summary and discussion are described in Section 5. We use the notation $Q_X = Q/10^X$ in cgs units unless otherwise noted and write Q' for the physical quantities in the comoving frame of the jet.

2. Neutrino Production Using Cocoon Photons

2.1. Photon Distributions

Neutrinos from GRBs are mainly produced by photomeson production. We consider that cosmic-ray (CR) protons are accelerated at a dissipation region in the jets. Photon distributions in the dissipation region affect the resulting neutrino spectra. Here, we consider two photon components: nonthermal radiation inside the jets and thermal radiation from the cocoon.

We write the differential number density of the nonthermal component using the Band function:

$$\frac{dn'^{\rm in}}{d\varepsilon'_\gamma} = n_{\varepsilon'_\gamma,{\rm nor}} \begin{cases} \varepsilon'^{\alpha}_\gamma \exp\left(-\dfrac{(2+\alpha)\varepsilon'_\gamma}{\varepsilon'_{\gamma,{\rm pk}}}\right) & (\varepsilon'_\gamma \leqslant \chi\varepsilon'_{\gamma,{\rm pk}}) \\ \varepsilon'^{\beta}_\gamma (\chi\varepsilon'_{\gamma,{\rm pk}}/e)^{\alpha-\beta} & (\varepsilon'_\gamma > \chi\varepsilon'_{\gamma,{\rm pk}}), \end{cases} \tag{1}$$

where α and β are the photon indices of X-rays below and above the peak, respectively, $\chi = (\alpha-\beta)/(2+\alpha)$, $n_{\varepsilon'_\gamma,{\rm nor}}$ is the normalization factor, and ε'_γ and $\varepsilon'_{\gamma,{\rm pk}}$ are the photon energy and the spectral peak energy in the jet comoving frame, respectively. The normalization is determined so that $L_{\rm X,iso} = 4\pi\Gamma_j^2 r_{\rm diss}^2 c \int_{\varepsilon_{\rm X,min}/\Gamma_j}^{\varepsilon_{\rm X,max}/\Gamma_j} d\varepsilon'_\gamma \varepsilon'_\gamma (dn'_\gamma/d\varepsilon'_\gamma)$ is satisfied, where $L_{\rm X,iso}$ is the isotropic-equivalent luminosity in the X-ray band, $r_{\rm diss}$ is the dissipation radius, Γ_j is the Lorentz factor of the jets, and $\varepsilon_{\rm X,max}$, and $\varepsilon_{\rm X,min}$ are the maximum and minimum energies of the X-ray band, respectively. Observationally, the X-ray luminosity shows a correlation with the duration of the extended emission as (Kisaka et al. 2017)

$$L_{\rm X,iso} = 2\times 10^{49}\left(\frac{t_{\rm dur}}{10^2\ {\rm s}}\right)^{-2.5} {\rm erg\ s^{-1}}. \tag{2}$$

We give $t_{\rm dur}$ as a parameter, and use the $L_{\rm X}$–$t_{\rm dur}$ relation to estimate the photon number density and the jet power. The total photon luminosity is obtained as $L_{\gamma,{\rm iso}} = 4\pi\Gamma_j^2 r_{\rm diss}^2 c \int_{\varepsilon'_{\gamma,{\rm min}}}^{\varepsilon'_{\gamma,{\rm max}}} d\varepsilon'_\gamma \varepsilon'_\gamma (dn'_\gamma/d\varepsilon'_\gamma)$, where $\varepsilon'_{\gamma,{\rm min}}$ and $\varepsilon'_{\gamma,{\rm max}}$ are the minimum and maximum photon energies, respectively. We set $\varepsilon'_{\gamma,{\rm min}} = 0.1$ eV and $\varepsilon'_{\gamma,{\rm max}} = 10^6$ eV because the synchrotron self-absorption and the pair creation are effective below and above the energies, respectively (Murase & Nagataki 2006b). The values of $\varepsilon'_{\gamma,{\rm min}}$ and $\varepsilon'_{\gamma,{\rm max}}$ do not strongly affect the results of this paper.

We use the one-zone approximation for the cocoon as discussed in Kimura et al. (2019). The cocoon temperature is obtained as $T_{\rm coc} = [3\mathcal{E}_{\rm coc}/(4\pi R_{\rm coc}^3 a_{\rm rad})]^{1/4}$, where $a_{\rm rad}$, $R_{\rm coc} = 3.0\times 10^{12}\, t_{\rm dur,2.5}$ cm, and $\mathcal{E}_{\rm coc}$ are the radiation constant, the cocoon radius, and the thermal energy of the cocoon, respectively. $\mathcal{E}_{\rm coc}$ is obtained as $\mathcal{E}_{\rm coc} = \mathcal{E}_{\rm adi} + \mathcal{E}_{\rm rad}$, where $\mathcal{E}_{\rm adi} = 8.8\times 10^{44} t_{\rm dur,2.5}^{-1}$ erg and $\mathcal{E}_{\rm rad} = 9.3\times 10^{44}\, t_{\rm dur,2.5}^{-0.3}$ erg represent the contributions from the initial thermal energy of ejecta and from the radioactive decay of neutron-rich nuclei in the ejecta.

The photons in the cocoon need to diffuse into the jet to work as an external photon field. Taking this effect into account, the spectrum of the thermal external photons entering the dissipation region from the cocoon is given by

$$\varepsilon'_\gamma \frac{dn'^{\rm ex}}{d\varepsilon'_\gamma} = \Gamma_j \frac{8\pi(\varepsilon'_\gamma/\Gamma_j)^3}{h^3c^3} \frac{1}{\exp\left[\varepsilon'_\gamma/(\Gamma_j k_{\rm B} T_{\rm coc})\right] - 1} \times e^{-\tau}, \tag{3}$$

where $T_{\rm coc}$ is the cocoon temperature, τ is the lateral optical depth of the jet, respectively, h is the Planck constant, $k_{\rm B}$ is the Boltzmann constant, and c is the speed of light. Hereafter, we call this component cocoon photons. The lateral optical depth is estimated to be $\tau = L_{k,{\rm iso}}\sigma_T\theta_j/(4\pi r_{\rm diss}\Gamma_j^2 m_p c^3) = 3.2\, L_{k,{\rm iso},50.5} r_{\rm dis,12}^{-1}\Gamma_{j,2}^{-2}(\theta_j/5^\circ)$, where σ_T, θ_j, and $L_{k,{\rm iso}}$ are the Thomson cross section, the opening angle of the jet, and the isotropic-equivalent kinetic luminosity, respectively. $L_{k,{\rm iso}}$ is estimated to be $L_{k,{\rm iso}} = L_{p,{\rm iso}}/\epsilon_p = \xi_p L_{\gamma,{\rm iso}}/\epsilon_p = 30(\xi_p/10)(\epsilon_p/0.33)^{-1} L_{\gamma,{\rm iso}}$, where $L_{p,{\rm iso}}$ is the luminosity of accelerated protons, and ξ_p and ϵ_p are parameters.

We ignore the cocoon photons for $R_{\rm coc} < r_{\rm diss}$ because the cocoon does not cover the dissipation region for such a condition. This is a rough approximation because the number of cocoon photons provided in the dissipation region should change smoothly, but it does not significantly affect the results because $R_{\rm coc} > r_{\rm diss}$ is satisfied in most cases in this study.

Recently, Hamidani & Ioka (2023) showed that a large fraction of cocoon is confined in the ejecta. If we apply the simulation to our model, $\mathcal{E}_{\rm coc}$ can be 200 times lower, and the temperature and number density of the cocoon photons can decrease by factors of $(1/100)^{1/4}$ and $(1/100)^{3/4}$, respectively. However, this effect does not change the results dramatically because the protons lose all the energies owing to a high cocoon photon density even for such a low temperature (see Equation (A5)).

2.2. Neutrino Spectra

Particle acceleration processes occurring in astrophysical environments usually lead to a power-law distribution function (e.g., Blandford & Eichler 1987; Guo et al. 2020), and we represent the CR distribution function in the rest frame of the engine as

$$\frac{dN_p}{d\varepsilon_p} = N_{\varepsilon_p,\rm nor}\left(\frac{\varepsilon_p}{\varepsilon_{p,\rm cut}}\right)^{-p_{\rm inj}}\exp\left(-\frac{\varepsilon_p}{\varepsilon_{p,\rm cut}}\right), \tag{4}$$

where $\varepsilon_{p,\rm cut}$ is the proton cutoff energy and $N_{\varepsilon_p,\rm nor}$ is the normalization factor. $N_{\varepsilon_p,\rm nor}$ is determined by $L_{p,\rm iso}t_{\rm dur} = \xi_p L_{\gamma,\rm iso}t_{\rm dur} = \int_{\varepsilon_{\rm min}}^{\infty} d\varepsilon_p \varepsilon_p (dN_p/d\varepsilon_p)$. The cutoff energy is determined by the balance between acceleration and cooling timescales. We use $\varepsilon_{p,\rm min} = \Gamma_j \varepsilon'_{\rm min} = 3\Gamma_j m_p c^2$ as the minimum energy of cosmic-ray protons, and ξ_p is the cosmic-ray loading parameter (Murase & Nagataki 2006a).

The acceleration timescale is estimated to be $t'_{\rm acc} = \varepsilon'_p/(ceB')$, where $B' = \sqrt{2L_{\gamma,\rm iso}\xi_B/(c\Gamma_j^2 r_{\rm diss}^2)}$ is the magnetic field in the comoving frame.

The cooling rate is given by $t'^{-1}_{\rm cool} = t'^{-1}_{\rm ad} + t'^{-1}_{\rm BH} + t'^{-1}_{p\gamma} + t'^{-1}_{\rm syn}$, where the terms represent adiabatic cooling, the Bethe–Heitler process, photomeson production, and synchrotron cooling, respectively. The adiabatic and the synchrotron cooling timescales are given by $t'_{\rm ad} = r_{\rm diss}/(\Gamma_j c)$ and $t'_{\rm syn} = 6\pi m_{\rm p}^4 c^3/(m_{\rm e}^2 \sigma_T B'^2)$, respectively. The cooling rates for Bethe–Heitler and photomeson production processes are estimated to be

$$t'^{-1}_{p\gamma/\rm BH} = \frac{c}{2\gamma'^2_p}\int_{\bar{\varepsilon}_{\rm th}}^{\infty} d\bar{\varepsilon}_\gamma \sigma(\bar{\varepsilon}_\gamma)\kappa(\bar{\varepsilon}_\gamma)\bar{\varepsilon}_\gamma \int_{\bar{\varepsilon}_\gamma/2\gamma_p}^{\infty} d\varepsilon'_\gamma \varepsilon'^{-2}_\gamma \frac{dn'_\gamma}{d\varepsilon'_\gamma}, \tag{5}$$

where $\gamma'_p = \varepsilon'_{\rm p}/(m_{\rm p}c^2)$ is the Lorentz factor of protons and $\bar{\varepsilon}_{\rm th}$, $\sigma(\bar{\varepsilon}_\gamma)$, and $\kappa(\bar{\varepsilon}_\gamma)$ are the threshold energy, the cross section, and the inelasticity for each reaction in the proton rest frame, respectively. We use the fitting formulae based on GEANT4 for the cross section and inelasticity for photomeson production (Murase & Nagataki 2006a) and analytic fitting formulae given in Stepney & Guilbert (1983) and Chodorowski et al. (1992) for the Bethe–Heitler process. We define $t_{p\gamma,\rm int}$, $t_{\rm BH,int}$, $t_{p\gamma,\rm coc}$, and $t_{\rm BH,coc}$ as the cooling timescales using the internal photons and the cocoon photons for the two processes, respectively.

The neutrino spectrum produced by the photomeson process and pion decay is approximately estimated to be

$$\frac{dN_{\nu_\mu}}{d\varepsilon_{\nu_\mu}} \approx \int d\varepsilon_\pi g(\varepsilon_\pi, \varepsilon_{\nu_\mu}) f_{\rm sup,\pi}\left(f_{p\gamma}\frac{dN_p}{d\varepsilon_p}\right)\Bigg|_{\varepsilon_p = 5\varepsilon_\pi} \tag{6}$$

for muon neutrinos, and

$$\frac{dN_{\bar{\nu}_\mu}}{d\varepsilon_{\bar{\nu}_\mu}} \approx \frac{dN_{\nu_e}}{d\varepsilon_{\nu_e}} \approx \int d\varepsilon_\mu g(\varepsilon_\mu, \varepsilon_{\nu_e}) f_{\rm sup,\mu}\left(f_{\rm sup,\pi} f_{p\gamma}\frac{dN_p}{d\varepsilon_p}\right)\Bigg|_{\varepsilon_p = 5\varepsilon_\pi = \frac{20}{3}\varepsilon_\mu} \tag{7}$$

for muon antineutrinos and electron neutrinos, where $f_{p\gamma} = t'_{\rm cool}/t'_{p\gamma}$, $f_{{\rm sup},i}$, and $g(\varepsilon_i, \varepsilon_j)d\varepsilon_j$ are the pion production efficiency by photomeson production, the suppression factor by the pion and muon coolings, and the distribution function of the secondary particle j produced by the decay of the parent particle i of energy ε_i, respectively. The suppression factor is estimated to be $f_{{\rm sup},i} = 1 - \exp(-t'_{i,\rm cool}/t'_{i,\rm dec})$, where $t'_{i,\rm dec}$ and $t'_{i,\rm cool}$ are the lifetime and the cooling timescale of each particle in the comoving frame of the jet, respectively. The lifetime is given by $t'_{i,\rm dec} = t_i \varepsilon'_i/(m_i c^2)$, where t_i is the lifetime in the particle rest frame, and m_i is the mass of a particle. $t'_{i,\rm cool}$ is estimated to be $t'^{-1}_{i,\rm cool} = t'^{-1}_{i,\rm syn} + t'^{-1}_{\rm ad}$, where $t'_{i,\rm syn} = 6\pi m_i^4 c^3/m_{\rm e}^2 \sigma_T B^2 \varepsilon'_i$. Here, we assume that all pions produced by the photomeson production with ε_p have $\varepsilon_\pi = 0.2\varepsilon_p$, and all muons produced by the decay of pions with ε_π have $\varepsilon_\mu = (3/4)\varepsilon_\pi$. We approximate $g(\varepsilon_\pi, \varepsilon_{\nu_\mu}) = 4\Theta(\varepsilon_\pi - 4\varepsilon_{\nu_\mu})/\varepsilon_\pi$ and $g(\varepsilon_\mu, \varepsilon_{\nu_e}) = 3\Theta(\varepsilon_\mu - 3\varepsilon_{\nu_e})/\varepsilon_\mu$, where $\Theta(x)$ is the Heaviside step function, because they imitate energy distributions for two-body decay. This treatment can approximately account for the low-energy tail of the neutrino spectrum, which would affect the detectability of neutrinos.

Taking account of the neutrino mixing, we can approximately obtain the neutrino fluences measured at the Earth as (e.g., Becker 2008)

$$\phi_{\nu_e+\bar{\nu}_e} \approx \frac{10}{18}\phi^0_{\nu_e+\bar{\nu}_e} + \frac{4}{18}(\phi^0_{\nu_\mu+\bar{\nu}_\mu} + \phi^0_{\nu_\tau+\bar{\nu}_\tau}) \tag{8}$$

$$\phi_{\nu_\mu+\bar{\nu}_\mu} \approx \frac{4}{18}\phi^0_{\nu_e+\bar{\nu}_e} + \frac{7}{18}(\phi^0_{\nu_\mu+\bar{\nu}_\mu} + \phi^0_{\nu_\tau+\bar{\nu}_\tau}), \tag{9}$$

where $\phi^0_i = (dN_i/d\varepsilon_i)/(4\pi d_L^2)$ is the neutrino fluence measured on Earth assuming that the flavor ratio is fixed at the source, and d_L is the luminosity distance.

Figure 1 shows the acceleration and cooling timescales of protons as a function of energy (see Table 1 for our fiducial parameter set for extended and plateau emission). For our extended emission models, the photomeson production is the most efficient cooling process for $\varepsilon'_p \gtrsim$ 10–100 TeV whereas adiabatic loss is the most efficient for $\varepsilon'_p \lesssim$ 10–100 TeV. The Bethe–Heitler process is not effective for any parameters due to its relatively low effective cross section. Synchrotron cooling is also not effective because of the large mass of a proton and the moderate magnetic field. For the plateau emission models, adiabatic loss is the most efficient except for $\varepsilon'_p \gtrsim 10$ PeV for $\Gamma_j = 10$; this is because of their lower cocoon photon density.

The fluences of $\nu_\mu + \bar{\nu}_\mu$ for the fiducial parameters and for some other parameters are shown in Figure 2. In Appendix appendix, we show an analytic expression of the fluence for the extended emission model with fiducial parameters (blue lines), which is dominated by cocoon photons. We also show the parameter dependence there.

For the cases with the other parameter sets shown in Figures 2(a) and (b), the neutrinos are mainly produced by

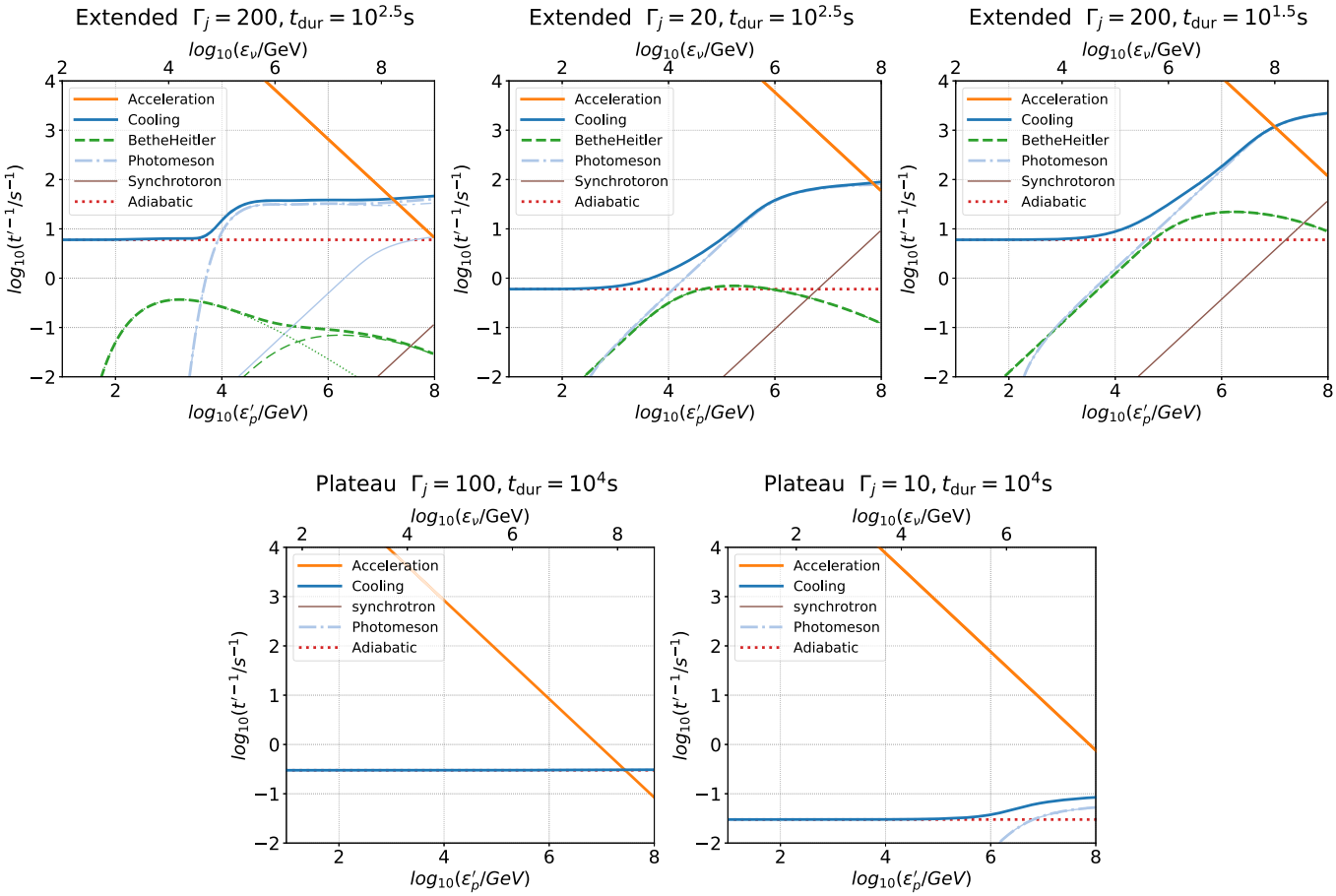

Figure 1. Acceleration and cooling rates for protons in the dissipation region in the comoving frame of the jet with various parameter sets. The thick orange lines and thick blue lines represent the acceleration timescales and total cooling timescales, respectively. The red thick dotted, the light blue thick dotted–dashed, and the green thick dashed lines represent $t'^{-1}_{\rm ad}$, $t'^{-1}_{p\gamma}$, and $t'^{-1}_{\rm BH}$, respectively. The light blue thin solid and the light blue thin dotted–dashed lines represent $t'^{-1}_{p\gamma,\rm int}$ and $t'^{-1}_{p\gamma,\rm coc}$, respectively. The green thin dashed and the green thin dotted lines represent $t'^{-1}_{\rm BH,int}$ and $t'^{-1}_{\rm BH,coc}$, respectively.

Table 1
Fiducial Parameters

Parameters	Γ_j	$t_{\rm dur}$ (s)	$L_{\rm X,iso}$ (erg s^{-1})	$r_{\rm diss}$ (cm)	$\varepsilon_{\gamma,\rm pk}$ (keV)
Extended	200	$10^{2.5}$	10^{48}	10^{12}	10
Plateau	100	10^{4}	10^{46}	10^{13}	1

Shared	α	β	$p_{\rm inj}$	ξ_p	ξ_B	$\varepsilon_{\rm X,min}$, $\varepsilon_{\rm X,max}$ (keV)	d_L (Mpc)
	−0.5	−2	2.0	10	0.33	0.3, 10 (XRT)	300

interaction with the internal photons. For $\Gamma_j = 20$ and $t_{\rm dur} = 10^{2.5}$, $\tau \sim 100$ is achieved, and the cocoon photons cannot diffuse into the dissipation region in such a high optical depth. For $\Gamma_j = 200$ and $t_{\rm dur} = 10^{1.5}$ s, $R_{\rm coc} < r_{\rm diss}$ is satisfied, and the cocoon photons cannot contribute to the neutrino emission. The neutrino spectra dominated by internal photons are roughly expressed by broken power-law shapes with an exponential cutoff that reflects the spectra of internal photons and protons.

The parameter dependence of these neutrino spectra is consistent with previous studies that consider only internal photons (Waxman & Bahcall 1998; Zhang & Kumar 2013; Kimura et al. 2017; Kimura 2022). The neutrino spectra exhibit two break points: the low-energy break due to the photon spectral break and the high-energy break due to the pion cooling. The relativistic beaming effect leads to $t^{-1}_{\rm ad} \propto \Gamma_j$ and $t^{-1}_{p\gamma,\rm int} \propto \Gamma_j^{-1}$, which can be seen in Figure 1 by comparing the top left and top middle panels. In this case, the neutrino fluence is written as $\phi_{\nu_\mu} \propto t^{-1}_{p\gamma,\rm int}/t^{-1}_{\rm ad} \propto \Gamma_j^{-2}$. We can see this dependence by comparing the peaks by internal photons for $\Gamma_j = 20$ (orange dashed line) and for $\Gamma_j = 200$ (blue thin dashed–dotted line) in Figure 2(a). For the case with $\Gamma_j = 200$ and $t_{\rm dur} = 10^{1.5}$ s, $t^{-1}_{p\gamma}$ and the fluence of neutrinos are much higher than those for other parameters, because we set the luminosity $10^{2.5}$ times higher than that for fiducial parameters based on Equation (2).

Neutrino fluences from plateau emissions are much lower than those for extended emissions. The difference between extended and plateau emissions is caused by the difference in the luminosity and the duration of the jet (see Table 1 for the difference between extended and plateau emission). For the plateau emission, the total energy of injected protons, $L_{\gamma,\rm iso}t_{\rm dur}$, is almost the same as that for extended emission. On the other hand, the photon number density for plateau emission is much less than that for extended emission because the longer duration leads to a low-temperature cocoon due to the expansion. This results in a low cocoon photon number density in the dissipation region, causing a lower neutrino production rate for plateau emissions.

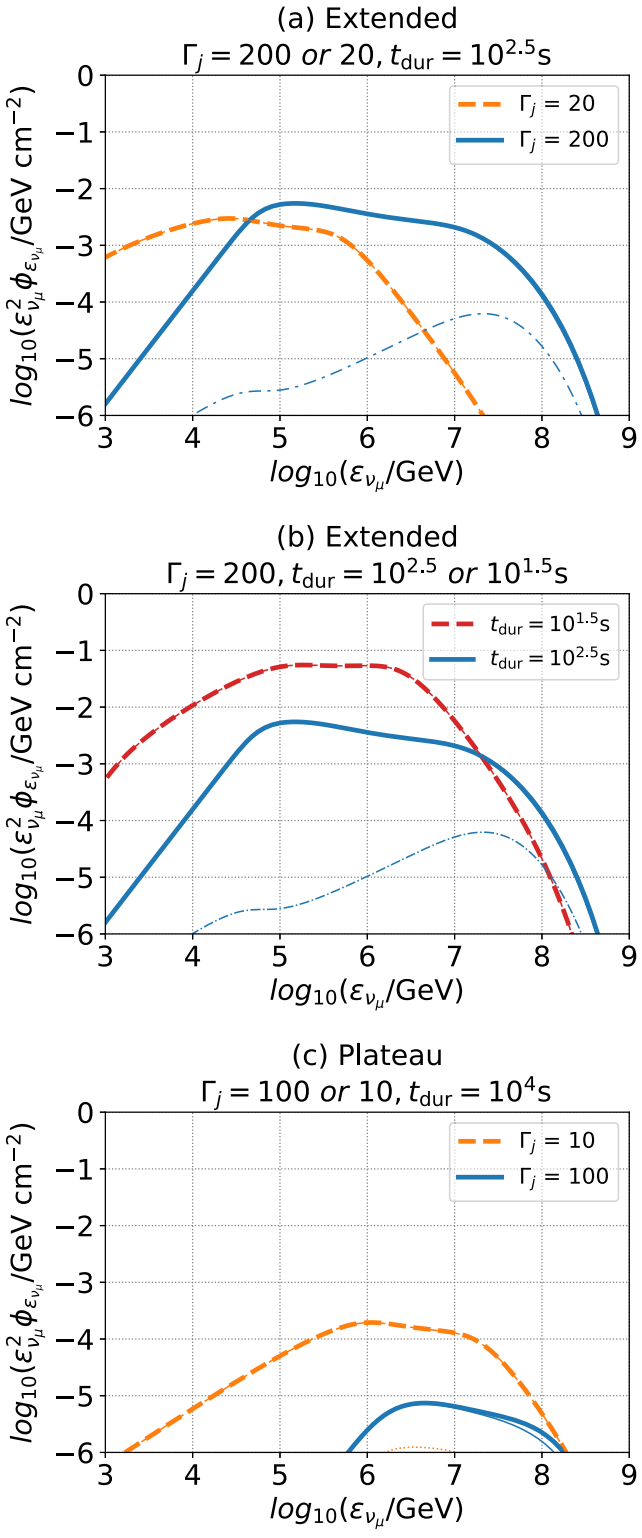

Figure 2. Neutrino fluences at the Earth. The thick lines are the total fluence and the thin lines are the contributions by the internal photons (in panels (a) and (b)) or cocoon photons (panel (c)). (a) Neutrino spectra for the extended emission models. The blue lines are for our fiducial parameter set, while the orange lines are for $\Gamma_j = 20$. The blue thin dotted–dashed line is the contribution from the internal photons. (b) Neutrino spectra for extended emission model. The blue lines are the same as in (a). The red line is for $t_{\rm dur} = 10^{1.5}$ s. (c) Neutrino spectra for plateau emission models. The blue lines are for our fiducial parameters, while the orange line is for $\Gamma_j = 10$.

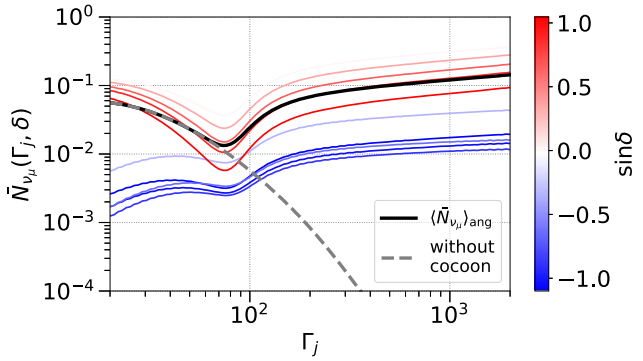

Figure 3. The expected number of ν_μ-induced events as a function of Γ_j (colored thin lines). The color bar represents the decl. angle. The black solid line represents the expected number averaged over the solid angle. The gray dashed line represents the expected number averaged over the solid angle without the cocoon photons.

3. Detection Prospects

We discuss prospects for neutrino detection associated with gravitational waves. Neutrino spectra from the extended emissions have a peak of $\sim 5.4 \times 10^{-3}$ GeV cm^{-2} at $\varepsilon_\nu \sim 1$ PeV, which is comparable to the design sensitivity for a transient object for IceCube-Gen2 (Aartsen et al. 2021). These neutrinos should be detectable if we stack multiple sGRBs with extended emission, which requires long-term operation. Since neutrinos from plateau emissions are too weak to be detected by near-future experiments, the following discussion focuses on the detectability of neutrinos from extended emissions.

3.1. Neutrino Detection from an sGRB

The expected number of ν_μ-induced events is estimated to be

$$\bar{N}_{\nu_\mu} = \int d\varepsilon_{\nu_\mu} \phi_{\nu_\mu + \bar{\nu}_\mu}(\varepsilon_{\nu_\mu}) A_{\rm eff}(\delta, \varepsilon_{\nu_\mu}), \quad (10)$$

where $A_{\rm eff}$ is the effective area of a detector and δ is decl. angle. We use $A_{\rm eff}$ given in the 10 yr point-source analysis (IceCube Collaboration et al. 2021), because this has a finer grid in δ than that used in the GRB analyses (Aartsen et al. 2017a). We assume that the effective area of IceCube-Gen2 is five times larger than that of IceCube.

We estimate $\bar{N}_{\nu_\mu}$ for various values of Γ_j and δ, and the results are shown in Figure 3. We use the fiducial parameters for other parameters, including $d_L = 300$ Mpc, as shown in Table 1. The gray dashed line represents the expected number averaged over the solid angle without the cocoon photons. This line is proportional to Γ_j^{-2} for $\Gamma_j < 100$ due to the Lorentz beaming effect, and to Γ_j^{-4} for $\Gamma_j > 100$ additionally because the low-energy break is higher than the energy range where IceCube is sensitive. The black solid line represents the expected number averaged over the solid angle with the cocoon photons. This line overlaps that without the cocoon photons for $\Gamma_j < 100$, since cocoon photons are negligible due to the shielding caused by large values of τ. For $\Gamma_j > 100$, the two lines separate from each other, due to the contribution of the cocoon photons. We find that if we take the cocoon photons into account, $\bar{N}_{\nu_\mu}$ has a relatively weak dependence on Γ_j, because the neutrino peak fluence does not depend strongly on

Γ_j when the cocoon photons are dominant, as shown in Appendix appendix. The expected number is slightly higher for a higher Γ_j because the muon and pion coolings are inefficient for a higher Γ_j.

The dependence on the decl. angle is caused by the effective area of IceCube. IceCube efficiently detects neutrinos from the equatorial plane. In the Southern Hemisphere, the low-energy neutrinos cannot be detected due to the atmospheric muons. In the Northern Hemisphere, the high-energy neutrinos are absorbed by the Earth, which reduces the neutrino detection rate. For low Γ_j, the main component is internal photons and the peak of neutrino fluence is lower than 1 PeV, where the atmospheric background is stronger. Thus, the value of $\bar{N}_{\nu_\mu}$ is lower for a lower Γ_j in the Southern sky although the peak fluence is higher as $\phi_{\nu_\mu} \propto \Gamma_j^{-2}$. The probability of detecting more than one neutrino is given by

$$p_{n\geqslant 1}(\delta) = 1 - \exp(-\bar{N}_{\nu_\mu}). \quad (11)$$

This probability depends on δ, and we calculate the probability averaged over the solid angle as[6]

$$\langle p_{n\geqslant 1}\rangle_{\rm ang} = \frac{1}{4\pi}\int d\Omega\, p_{n\geqslant 1}(\delta). \quad (12)$$

We calculate $\langle p_{n\geqslant 1}\rangle_{\rm ang}$ for various $t_{\rm dur}$ by using Equation (2), and find that $\langle p_{n\geqslant 1}\rangle_{\rm ang}$ depends strongly on $t_{\rm dur}$ as shown in Figure 4. There is a jump at $t_{\rm dur} = 10^2$ s for $\Gamma_j = 2000$, caused by the condition of no cocoon photons, $R_{\rm coc} = \beta_{\rm coc} c t_{\rm dur} < r_{\rm diss}$. The jump is an artifact because the number density of the cocoon photons in the dissipation region should change more smoothly. The bump at $t_{\rm dur} \sim 200$ s for $\Gamma_j = 200$ is caused by the shielding of cocoon photons due to the high optical depth. For $t_{\rm dur} > 100$ s, the expansion of the cocoon decreases the cocoon temperature and the photon number density, leading to a low neutrino fluence for a high value of $t_{\rm dur}$. For $t_{\rm dur} < 100$ s, the internal photons dominate because $r_{\rm diss} > R_{\rm coc}$ is satisfied, and $\langle p_{n\geqslant 1}\rangle_{\rm ang}$ is high for a low value of $t_{\rm dur}$ because $L_{\rm X,iso} \propto (t_{\rm dur}/10^2\ {\rm s})^{-2.5}$.

3.2. Prospects for Detecting Neutrinos Associated with GWs

We estimate the expected number of neutrino detections associated with GWs, taking into account the distribution of $t_{\rm dur}$ and $L_{\rm X,iso}$. We assume that the distribution of $t_{\rm dur}$ is log-normal:

$$F(t_{\rm dur}) = \frac{dN_{t_{\rm dur}}}{d\log_{10}(t_{\rm dur})} = F_0 \exp\left(-\frac{(\log_{10}(t_{\rm dur}/t_{\rm dur,0}))^2}{2\sigma^2_{\log_{10} t_{\rm dur}}}\right), \quad (13)$$

where $t_{\rm dur,0}$ and $\sigma^2_{\log_{10} t_{\rm dur}}$ are the mean and variance of the duration, respectively. We fit the data of extended emission listed in Kisaka et al. (2017) to obtain the values of $t_{\rm dur,0} = 10^{2.4}$ s and $\sigma^2_{\log_{10} t_{\rm dur}} = 8.3 \times 10^{-2}$.

The probability of detecting neutrinos from an sGRB is given by

$$P_{n\geqslant 1} = \int d(\log_{10} t_{\rm dur}) F(t_{\rm dur}) \langle p_{n\geqslant 1}\rangle_{\rm ang}. \quad (14)$$

We show the dependence of $P_{n\geqslant 1}$ on d_L in Figure 5. The behavior of the line for each Γ_j is roughly the same for each d_L.

[6] The probability differs from $p_{n\geqslant 1}(\langle \bar{N}_{\nu_\mu}\rangle_{\rm ang}) = 1 - \exp[-\int d\Omega \bar{N}_{\nu_\mu}/(4\pi)]$.

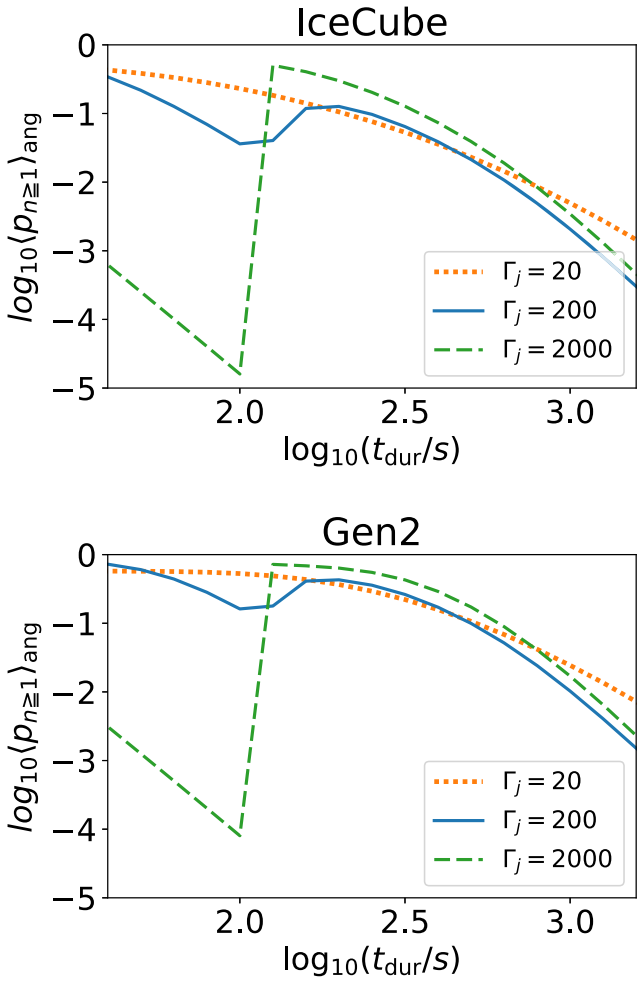

Figure 4. The probability of detecting more than one neutrino as a function of $t_{\rm dur}$. The upper and lower panels are the models for IceCube and IceCube-Gen2, respectively. The dotted, solid, and dashed lines represent the probability for $\Gamma_j = 20$, 200, and 2000, respectively.

$P_{n\geqslant 1} \propto d_L^{-2}$ for high d_L is consistent with $\phi_{\nu_\mu} \propto d_L^{-2}$ for a fixed luminosity. Assuming the uniform distributions of the location and timing of sGRBs, we can estimate the probability of detecting more than one neutrino associated with a GW signal in $T_{\rm op}$ (yr) to be

$$q(T_{\rm op}) = 1 - \exp\left(-T_{\rm op} R_{\rm sGRB} 4\pi \int^{300{\rm Mpc}} d(d_L) d_L^2 P_{n\geqslant 1}\right), \quad (15)$$

where $R_{\rm sGRB} = 8\ {\rm Gpc}^{-3}\ {\rm yr}^{-1}$ is the event rate of sGRBs (e.g., Coward et al. 2012).

The relation between q and $T_{\rm op}$ for IceCube (the thick lines) and for IceCube-Gen2 (the thin lines) is shown in Figure 6. We can constrain our fiducial parameter set for 2σ (3σ) confidence level within $\sim$10 ($\sim$15) yr of operation by IceCube-Gen2, although it would take more than 25 yr by IceCube even for the most optimistic case. This indicates the importance of IceCube-Gen2 for detecting neutrinos from sGRBs and revealing the characteristics of prolonged jets.

We set the maximum luminosity distance as 300 Mpc, taking into account the sensitivity limit of BNS mergers for second-generation GW detectors. Then, $R_{\rm sGRB}$ should be the rate of local sGRBs although it has large uncertainty due to the low

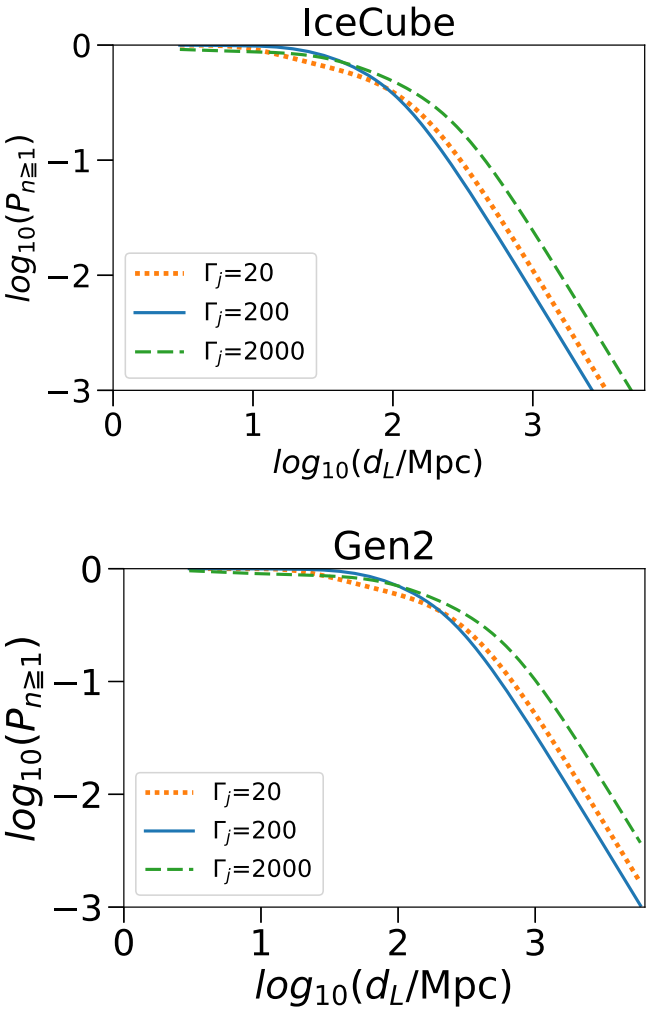

Figure 5. The probability of detecting more than one neutrino as a function of d_L. The upper and lower panels are models for IceCube and IceCube-Gen2, respectively. The dotted, solid, and dashed lines represent probability for $\Gamma_j = 20$, 200, and 2000, respectively.

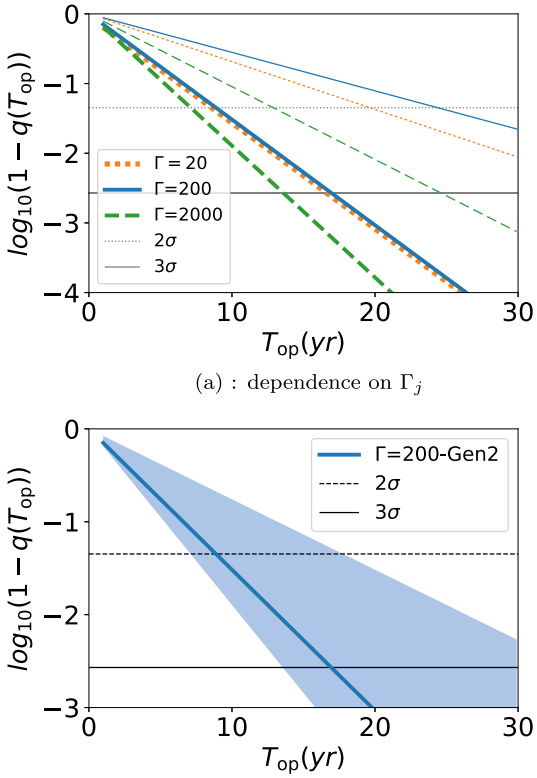

Figure 6. The probability of neutrino detection against the operation time. The thin horizontal lines correspond to significances of 2σ and 3σ. (a) Thick and thin lines represent the models for IceCube and IceCube-Gen2, respectively. The dotted, solid, and dashed lines represent probability for $\Gamma_j = 20$, 200, and 2000, respectively. (b) The uncertainty for the local sGRB rate. The colored region corresponds to the probability between the cases with $R_{\rm sGRB} = 4\ \mathrm{Gpc^{-3}\ yr^{-1}}$ and with $R_{\rm sGRB} = 10\ \mathrm{Gpc^{-3}\ yr^{-1}}$.

number of local sGRBs (Wanderman & Piran 2015; Rouco Escorial et al. 2022). Figure 6(b) shows that the result is sensitive to the rate, but the possibility becomes equivalent to 2σ within 20 yr of operation. We need to determine the local sGRB rate to make a more solid prediction for neutrino detection. In 20 yr, the development of GW observatories will enable us to observe BNS mergers from far more than 300 Mpc. This will dramatically increase the number of GW events, which will possibly lead to an earlier detection of a neutrino associated with a GW event.

4. GRB 211211A

GRB 211211A is a long GRB whose prompt emission lasts for 13 s and is followed by a soft extended component with a duration of 55 s (Yang et al. 2022). The progenitor of the GRB, however, is thought to be a merger of compact objects. Its host galaxy candidate is located at $d_L \simeq 350$ Mpc, and the GRB occurred in the outskirts of the galaxy. The prompt burst exhibits typical observational features of sGRBs, such as the negligible temporal lag, short variability timescale, and the position of the $\varepsilon_{\gamma,\rm pk}$–$E_{\rm iso}$ relation (Troja et al. 2022). The tentative evidence of a kilonova associated with the GRB also supports the BNS merger origin (Rastinejad et al. 2022).

Additionally, GeV gamma rays are observed with the GRB 10^3–10^4 s after the prompt emission (Mei et al. 2022). The gamma rays are explained by the external inverse Compton scattering process by nonthermal electrons accelerated in a prolonged jet (see Zhang et al. 2022 for another interpretation). Although the GeV signature is observed at a much later phase than the extended emission, the same system might be realized during the extended emission phase.

Neutrino associations with the GRB have not been reported by a gamma-ray follow-up (GFU) search of IceCube. This implies that we can obtain an upper limit on the neutrino flux from the GRB using the effective area of the GFU (Aartsen et al. 2017b).

In Section 2.2, we show that neutrino emission with plateau emission is not detectable by IceCube and IceCube-Gen2. This is consistent with the nondetection of neutrinos. On the other hand, it is expected that neutrinos could be found with extended emission because the extended emission is much more luminous than the plateau emission. To check the consistency of our model, we calculate $\bar{N}_{\nu_\mu}$ from GRB 211211A based on our scenario.

The properties of the event and its extended emission are summarized in Table 2 (see Table 1 of Yang et al. 2022 for other quantities). Since the duration of the extended emission is relatively short, the dissipation radius should be small, $r_{\rm diss} \lesssim 5.3 \times 10^{11}$ cm, for the cocoon photons to enter dissipation regions. The calculations are performed by setting $\Gamma = 10$–5000 and $r_{\rm diss} = 10^{10}$–10^{13} cm though they include extreme parameters. The results are shown in Table 3 and Figure 7. These indicate that the expected numbers of neutrinos observed by IceCube are less

Table 2
Properties of GRB 211211A

R.A.		Decl. ($=\delta$)	
$14^{h}09^{m}05^{s}$		$+27°53'01''$	
t_{dur} (s)	$\varepsilon_{\gamma,pk}$ (keV)	α	β
55	82	−0.97	−2.02
Energy Fluence (erg cm^{-2})	$L_{X,iso}$ (erg s^{-1})	$\varepsilon_{X,min}$, $\varepsilon_{X,max}$ (keV)	d_L (Mpc)
1.6×10^{-4}	4.3×10^{49}	15, 150 (BAT)	350

than 1 for all the parameter sets. The expected number for the GFU is also less than 1 because the effective area of the GFU is smaller than that of the point source in the Northern Hemisphere ($\delta > 0$). These results are consistent with the absence of GFU alerts associated with GRB 211211A. We cannot constrain the parameter space with the current facilities.

The observation by IceCube-Gen2 is important. The circles in Figure 7 show parameters where the calculated numbers of neutrinos expected by IceCube are greater than 0.2. The effective area of IceCube-Gen2 is five times larger than that of IceCube, and IceCube-Gen2 will be able to detect a neutrino from GRB 211211A-like bursts for those parameters or put a constraint on the 68% confidence level.

The neutrino signals from GRB 211211A are stronger for region of low Γ_j owing to the intense internal photon field. The neutrino signals can be stronger for a region of medium r_{diss} and high Γ_j because of the cocoon photons. These results can be analytically understood from the following discussion.

First, we discuss the conditions when the internal photons are dominant. For efficient neutrino production, the pion production efficiency needs to be high. Considering the large effective area of IceCube around $\varepsilon_{\nu_\mu} \sim 100$ TeV, the condition for efficient pion production is determined by $(t'_{ad}/t'_{p\gamma,int})|_{\varepsilon_\nu = 100\ \mathrm{TeV}} \geqslant 1$. This condition can be represented as

$$r_{dis,12} \leqslant 6.0\ \Gamma_{j,2}^{-2} L_{\gamma,iso,50} \left(\frac{\varepsilon_{\gamma,pk}}{100\ \mathrm{keV}}\right)^{-1} \times \left[1 + 0.54 \left(\frac{\varepsilon_{\gamma,pk}}{100\ \mathrm{keV}}\right) \Gamma_{j,2}^{2}\right]^{-1}, \quad (16)$$

which is derived from Equation (28) in Kimura (2022). This condition is shown by the red solid line in Figure 7. In addition, the pion cooling needs to be inefficient. The condition for inefficient pion cooling is determined by $\varepsilon_{\nu,cool} \geqslant 100$ TeV, where $\varepsilon_{\nu,cool}$ is defined by $(t'_{\pi,cool}|_{\varepsilon'_p = 20\varepsilon_{\nu,cool}/\Gamma_j} / t'_{\pi,dec}|_{\varepsilon'_p = 20\varepsilon_{\nu,cool}/\Gamma_j}) = 1$. The condition leads to

$$r_{dis,12} \geqslant 4.6 \times 10^{-3}\ \Gamma_{j,2}^{-2} L_{\gamma,iso,50}^{1/2} \left(\frac{\xi_B}{0.33}\right)^{1/2} + 2.5 \times 10^{-3}. \quad (17)$$

The first term on the right-hand side is the contribution from synchrotron cooling and the second is from adiabatic cooling. The red dotted line represents this condition.

Next, we consider the case where the cocoon photons are dominant. For efficient neutrino production, the cocoon needs to cover the dissipation region, $r_{diss} \leqslant R_{coc}$, which is shown as the blue solid line. If this condition is satisfied, the cocoon photons always lead to efficient neutrino production, i.e., $(t'_{ad}/t'_{p\gamma,coc})|_{peak} \geqslant 1$. The cocoon photons are shielded if the lateral optical depth, τ, is large. Strong shielding can be avoided if $e^{-\tau} \geqslant 1/10$ is satisfied. This condition can be rewritten as

$$r_{dis,12} \geqslant 40 \times \Gamma_{j,2}^{-2} L_{\gamma,iso,50} \times \ln 10. \quad (18)$$

This condition is shown by the blue dashed line.

In summary, neutrino production is efficient below the solid lines and above the dashed lines in Figure 7. In the red shaded region, the neutrinos are produced by the internal photons, whereas the cocoon photons are important in the blue shaded region.

5. Summary and Discussion

We calculated the neutrino fluence emitted by the prolonged jet of an sGRB, which can be associated with a GW event. We take into account the photons entering the jet from the cocoon formed by the jet–ejecta interaction. Owing to the contribution from the cocoon photons, the peak neutrino fluence has a weak dependence on the Lorentz factor of the jet, Γ_j. We found that the peak fluence is approximately 5.4×10^{-3} GeV cm^{-2} at $\varepsilon_\nu \sim 1$ PeV from a single sGRB with our fiducial parameters shown in Table 1. We expect that the number of neutrino events expected by IceCube will be 0.1, while that expected by IceCube-Gen2 will be 0.5. Assuming a homogeneous spatial distribution and a log-normal distribution of duration of sGRBs, we found that the possibility of neutrino detection associated with GW events is sufficiently high if we continue to observe cosmic neutrinos with IceCube-Gen2 for 10 years. Even if the future observation results in no detection of neutrinos associated with GWs, we can put a strong constraint on the parameter space of the late-time jets. We also applied our model to GRB 211211A. We found that no neutrino signal in IceCube associated with GRB 211211A is consistent with our model, but we can put a meaningful constraint on future GRB 211211A-like events if IceCube-Gen2 is in operation.

We assumed that CRs are accelerated at the dissipation radius, but we need to be cautious about the condition for CR production. In the internal shock model, a radiation-mediated shock can be formed if the upstream region of the shock is optically thick, which prevents CRs from being accelerated (Murase & Ioka 2013; Kimura et al. 2018). This effect can drastically reduce neutrino fluence. However, our scenario can avoid the condition even for $\Gamma_j = 20$ as long as the Lorentz factor of the shock upstream is as high as 100.

In addition, we should note that the energy density of the internal photon, $\int_{\varepsilon_{X,min}/\Gamma_j}^{\varepsilon_{X,max}/\Gamma_j} d\varepsilon'_\gamma \varepsilon'_\gamma (dn'_\gamma/d\varepsilon'_\gamma) = L_{X,iso}/(4\pi\Gamma_j^2 r_{diss}^2 c)$, can be modified if $\tau_j > 1$ is satisfied. The internal photon density can be constant in radius if some of the kinetic energy of the jet dissipates inside the photosphere, as discussed in Rees & Mészáros (2005). In this case, our results are not affected. However, the photon luminosity in the dissipation region can be higher than that in the photosphere if the dissipation cannot compensate for the energy loss caused by the adiabatic expansion. In this case, the internal photon density in the dissipation region is higher than that in the photosphere. Nevertheless, this effect has little influence on the neutrino fluence because of the efficient neutrino production, $f_{p\gamma} = 1$, for the cases with $\tau_j \gtrsim 1$. Therefore, our conclusions should be unchanged as long as CRs are accelerated at the given r_{diss}.

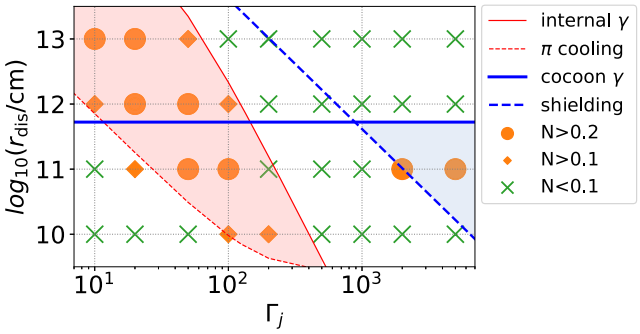

Figure 7. The chart of neutrino number from GRB 211211A. The orange circles, orange diamonds, and green crosses indicate the parameters for $0.2 < \bar{N}_{\nu_\mu}$, $0.1 < \bar{N}_{\nu_\mu} < 0.2$, and $\bar{N}_{\nu_\mu} < 0.1$, respectively. The red solid and blue solid lines indicate the boundary for efficient pion production by internal and cocoon photons, respectively. The red dashed line is the boundary for efficient pion cooling, and the blue dashed line is the boundary for the shielding of the cocoon photons. Red shaded and blue shaded regions are the areas of parameter space where neutrinos are efficiently produced by internal and cocoon photons, respectively.

We can constrain other parameters, such as dissipation radius $r_{\rm diss}$, more strongly than the previous study if we ignore the dependence on Γ_j. The case with $r_{\rm diss} > 10^{12}$ cm will favor the internal shock model or internal collision-induced magnetic reconnection and turbulence (Zhang & Yan 2011; Zhang & Kumar 2013), while the case with $r_{\rm diss} < 10^{12}$ cm would favor the scenario of a dissipative photosphere (Rees & Mészáros 2005).

The detection of neutrinos from sGRBs will be a smoking-gun signature of hadronic CR acceleration in the sGRB environment. This can constrain the composition of the jet in extended emission, i.e., whether prolonged jets are leptonic or baryonic. Baryonic jets demand a baryon injection process into them, such as neutron diffusion from neutron-rich matter (Beloborodov 2003; Levinson & Eichler 2003), which is thought to be the process of baryon injection into prompt jets. In the phase of late-time emission, the mass accretion rate onto the remnant object might be too low to form neutron-rich material (e.g., Kohri et al. 2005). Magnetar models are often discussed as a possible explanation of extended emissions only by the leptonic process (Dai & Lu 1998). Neutrino observations will potentially be able to rule out some leptonic models, which will clarify the jet launching mechanism.

Abbasi et al. (2022) conclude that time-integrated fluences 300 s after the event for all northern sGRBs (183 events) are less than 1×10^{-1} GeV cm^{-2} in total by analyzing the correlation of the GRB catalog detected by Swift or Fermi and IceCube data sets. This means that the upper limit on the fluence from a single sGRB is about 5×10^{-4} GeV cm^{-2} on average. The data include mostly the signals of sGRBs from cosmological distance, which is not the focus of our study. If we assume that the redshifts of the sGRBs analyzed in Abbasi et al. (2022) are typically about $z \sim 0.5$ (corresponding to $d_L \sim 3$ Gpc), the upper limit on neutrino luminosity becomes about 3×10^{48} erg s^{-1}. The neutrino luminosity in our model, $\sim 5 \times 10^{47}$ erg s^{-1}, is lower than the upper limit and consistent with the IceCube data.

The high-energy gamma-ray observations also provide a test for our model. The astrophysical neutrinos are inevitably accompanied by gamma rays produced by π^0 decay with a similar energy and luminosity, because the reaction rate of π^0 production is almost the same as that of $\pi^\pm$ production. However, the peak energy of gamma rays is not 100 TeV–1 PeV, because they will cascade into lower energies by interaction with low-energy photons. The resulting peak of the escaped photon spectrum is expected to be between a few MeV and a few GeV. Gamma rays in this energy band will be detected by future telescopes, such as eASTROGAM (De Angelis et al. 2017), GRAMS (Aramaki et al. 2020), and AMEGO-X (Caputo et al. 2022). The multimessenger approach, using gamma-ray and neutrino signals, will be a powerful tool to constrain the physical conditions of the dissipation region.

Table 3
Expected Number of Neutrinos from GRB 211211A

$r_{\rm dis}$ (cm)	$\Gamma_j = 20$	$\Gamma_j = 200$	$\Gamma_j = 2000$
10^{13}	4.1×10^{-1}	5.3×10^{-3}	9.1×10^{-7}
10^{12}	3.0×10^{-1}	2.7×10^{-2}	6.0×10^{-6}
10^{11}	1.2×10^{-1}	7.5×10^{-2}	8.2×10^{-1}
10^{10}	2.1×10^{-2}	1.0×10^{-1}	1.1×10^{-4}

Neutrino detection associated with GWs enables us to probe phenomena that cannot be investigated by EM signals alone. Choked jet systems, where jets fail to break out from the stellar envelope or kilonova ejecta, are a good example (Murase & Ioka 2013; Kimura et al. 2018). The threshold timescale in the distribution of duration of prompt emissions of sGRBs indicates the existence of such events (Moharana & Piran 2017). Matsumoto & Kimura (2018) showed that a prolonged jet can break out from the ejecta even if a prompt jet fails to penetrate it. In such a scenario, we cannot observe the emission from prompt jets but can observe the extended emission from prolonged jets. X-ray observations found a few candidates for such a delayed breakout event (Xue et al. 2019), but they are difficult to confirm. Based on our model, we expect detection of neutrinos and GWs from the delayed breakout event. Thus, GW–neutrino association without prompt gamma rays would strongly support the scenario of the delayed breakout. The event rate of choked jets is expected to be approximately 0.4 times lower than that of successful sGRBs (Sarin et al. 2022), although it can be increased by the uncertainty of the event rate of sGRBs and BNS mergers. If the fraction of choked jets is at the high end, the delayed breakout will be a major component, and we will be able to detect much more GW–neutrino association. Thus, GW–neutrino association can be a powerful tool to probe the activity of the central engine.

Acknowledgments

This work is supported by Graduate Program on Physics for the Universe (GP-PU), Tohoku University (R.M.), JSPS KAKENHI No. 22K14028 (S.S.K.) and 18H01245 (K.T.). This work of K.M. is supported by the NSF Grant No. AST-1908689, No. AST-2108466 and No. AST-2108467, and KAKENHI No. 20H01901 and No. 20H05852. S.S.K. acknowledges the support by the Tohoku Initiative for Fostering Global Researchers for Interdisciplinary Sciences (TI-FRIS) of MEXT's Strategic Professional Development Program for Young Researchers.

Appendix A
Analytic Explanation of Neutrino Spectra

In this appendix, we analytically estimate the neutrino fluence when cocoon photons dominate over internal photons. If we assume $g(\varepsilon_\pi, \varepsilon_{\nu_\mu}) = \delta(\varepsilon_\pi/4 - \varepsilon_{\nu_\mu})$ and $g(\varepsilon_\mu, \varepsilon_{\nu_e})=$

$\delta(\varepsilon_\mu/3 - \varepsilon_{\nu_e})$, the neutrino spectra are given by

$$\varepsilon_{\nu_\mu}^2 \frac{dN_{\nu_\mu}}{d\varepsilon_{\nu_\mu}} \approx \frac{1}{8} f_{p\gamma} f_{\mathrm{sup},\pi} \varepsilon_p^2 \frac{dN_p}{d\varepsilon_p}\Bigg|_{\varepsilon_p = 20\varepsilon_{\nu_\mu}} \tag{A1}$$

$$\varepsilon_{\bar{\nu}_\mu}^2 \frac{dN_{\bar{\nu}_\mu}}{d\varepsilon_{\bar{\nu}_\mu}} \approx \varepsilon_{\nu_e}^2 \frac{dN_{\nu_e}}{d\varepsilon_{\nu_e}} \approx \frac{1}{8} f_{p\gamma} f_{\mathrm{sup},\pi} f_{sup,\mu} \varepsilon_p^2 \frac{dN_p}{d\varepsilon_p}\Bigg|_{\varepsilon_p = 20\varepsilon_{\nu_\mu}}. \tag{A2}$$

These are useful for understanding the resulting spectrum analytically (e.g., Kimura 2022, for a review). This expression assumes that all the decay products produced by a pion with ε_π share the same amount of energy: $\varepsilon_{\nu_\mu} \approx \varepsilon_{\nu_e} \approx \varepsilon_{\bar{\nu}_\mu} \approx \varepsilon_e \approx \varepsilon_\pi/4$.

To estimate $f_{p\gamma}$ and the fluence, we can roughly estimate $t'_{p\gamma}$ by using additional approximations. Considering only cocoon photons, which are the dominant component for the fiducial parameters, and $\sigma\kappa \sim \sigma_{0,\mathrm{eff}}\theta(\bar{\varepsilon}_\gamma - \bar{\varepsilon}_{\mathrm{th}})$ as an approximation, we can perform the calculation of Equation (5). Using Equation (69) of Dermer et al. (2012), we can obtain the timescale of photomeson production with the cocoon photons as

$$t'^{-1}_{p\gamma,\mathrm{coc}} = \frac{16\pi k_{\mathrm{B}}^3 T_{\mathrm{coc}}^3 \sigma_{0,\mathrm{eff}}}{h^3 c^2}\Gamma_j \int_{\tilde{\varepsilon}'_p/\varepsilon'_p}^{\infty} dy\, y \ln(1 - e^{-y})^{-1} \sim \frac{16\pi k_{\mathrm{B}}^3 T_{\mathrm{coc}}^3 \sigma_{0,\mathrm{eff}}}{h^3 c^2}\Gamma_j \begin{cases} \zeta(3) & (\varepsilon'_p \gg \tilde{\varepsilon}'_p) \\ \tilde{\varepsilon}'_p/\varepsilon'_p\, e^{-\tilde{\varepsilon}'_p/\varepsilon'_p} & (\varepsilon'_p \ll \tilde{\varepsilon}'_p), \end{cases} \tag{A3}$$

where $\tilde{\varepsilon}'_p = (\bar{\varepsilon}_{\mathrm{th}} m_p c^2)/(2k_{\mathrm{B}} T_{\mathrm{coc}}\Gamma_j)$ is the threshold energy of protons for photomeson production with typical cocoon photons, and $\zeta(x)$ is the zeta function. The light blue thin dotted–dashed line shown in Figure 1, which almost completely overlaps the thick dotted–dashed line in our fiducial model, can be well explained by this approximate formula. $t'^{-1}_{p\gamma,\mathrm{coc}}$ is constant for $\varepsilon'_p \gtrsim \tilde{\varepsilon}'_p$, and it has an exponential cutoff at lower energies. The cutoff neutrino energy in the observer frame is estimated to be

$$\varepsilon_\nu \sim \frac{\tilde{\varepsilon}'_p}{20\Gamma_j} = \frac{\bar{\varepsilon}_{\mathrm{th}} m_p c^2}{40 k_{\mathrm{B}} T_{\mathrm{coc}}} \sim 0.13\left(\frac{\bar{\varepsilon}_{\mathrm{th}}}{0.1\ \mathrm{GeV}}\right)\left(\frac{k_{\mathrm{B}} T_{\mathrm{coc}}}{20\ \mathrm{eV}}\right)^{-1} \mathrm{PeV} \tag{A4}$$

which does not depend on Γ_j.

For $\varepsilon'_p > \tilde{\varepsilon}'_p$, we can write

$$t'^{-1}_{p\gamma,\mathrm{coc}} \sim 88\left(\frac{\sigma_{0,\mathrm{eff}}}{6 \times 10^{-29}\ \mathrm{cm}^2}\right)\left(\frac{k_{\mathrm{B}} T_{\mathrm{coc}}}{20\ \mathrm{eV}}\right)^3\left(\frac{\Gamma_j}{200}\right)\ \mathrm{s}^{-1}. \tag{A5}$$

Based on Figure 1, the photomeson production with cocoon photons is the most efficient process, and all the protons with $\varepsilon'_p > \tilde{\varepsilon}'_p$ lose their energy. Thus, the peak fluence contributed by cocoon photons does not depend on Γ_j. Even for the case with $t'_{\mathrm{ad}} < t'_{p\gamma,\mathrm{coc}}$, both of the timescales have the same Γ_j dependence, and therefore the pion production efficiency and the neutrino fluence do not depend on Γ_j as long as the cocoon photons are dominant for neutrino production.

The high-energy cutoff in the neutrino spectra is caused by the proton injection spectrum. The cutoff energy of protons in the observer frame depends on Γ_j. In the range, $t'^{-1}_{\mathrm{cool}} \sim t'^{-1}_{p\gamma,\mathrm{coc}} \propto \Gamma_j$ is satisfied and t'^{-1}_{acc} is proportional to Γ_j^{-1} due to Lorentz transformation of the magnetic field. This leads to $\varepsilon'_{p,\mathrm{cut}} \propto \Gamma_j^{-2}$ and $\varepsilon_{p,\mathrm{cut}} \propto \Gamma_j^{-1}$. The cutoff energy is $\varepsilon'_{p,\mathrm{cut}} \sim 8.2 \times 10^6\ (\Gamma_j/200)^{-2}$ GeV for the proton energy in the comoving frame of the jet and $\varepsilon_\nu \sim 8.2 \times 10^7\ (\Gamma_j/200)^{-1}$ GeV for neutrino energy in the observer frame for the fiducial parameters.

For $\varepsilon_{\nu_\mu} < 100$ TeV, the resultant fluence shown in Figure 2 is $\varepsilon_\nu^2(dN_\nu/d\varepsilon_\nu) \propto \varepsilon_\nu^2$, while $f_{p\gamma,\mathrm{coc}} \times \varepsilon_p^2(dN_p/d\varepsilon_p)$ should have a cutoff feature. This is because of the different treatment of $g(\varepsilon_i, \varepsilon_j)$. The cutoff feature of the lower energy is not realistic since decaying pions with the peak energy must produce neutrinos with energies lower than $(1/4)\varepsilon_\pi$.

ORCID iDs

Riki Matsui https://orcid.org/0000-0003-0805-7741
Shigeo S. Kimura https://orcid.org/0000-0003-2579-7266
Kenji Toma https://orcid.org/0000-0002-7114-6010
Kohta Murase https://orcid.org/0000-0002-5358-5642

References

Aartsen, M. G., Abbasi, R., Abdou, Y., et al. 2013, PhRvL, 111, 021103
Aartsen, M. G., Abbasi, R., Ackermann, M., et al. 2021, JPhG, 48, 060501
Aartsen, M. G., Abraham, K., Ackermann, M., et al. 2016, ApJ, 824, 115
Aartsen, M. G., Ackermann, M., Adams, J., et al. 2015, ApJL, 805, L5
Aartsen, M. G., Ackermann, M., Adams, J., et al. 2017a, ApJ, 843, 112
Aartsen, M. G., Ackermann, M., Adams, J., et al. 2017b, APh, 92, 30
Aartsen, M. G., Ackermann, M., Adams, J., et al. 2020, PhRvL, 124, 051103
Abbasi, R., Abdou, Y., Abu-Zayyad, T., et al. 2010, ApJ, 710, 346
Abbasi, R., Abdou, Y., Abu-Zayyad, T., et al. 2011, PhRvL, 106, 141101
Abbasi, R., Ackermann, M., Adams, J., et al. 2022, ApJ, 939, 116
Abbott, B. P., Abbott, R., Abbott, T. D., et al. 2017a, ApJL, 848, L12
Abbott, B. P., Abbott, R., Abbott, T. D., et al. 2017b, PhRvL, 119, 161101
Abbott, B. P., Abbott, R., Abbott, T. D., et al. 2017c, ApJL, 848, L13
Agostini, M., Böhmer, M., Bosma, J., et al. 2020, NatAs, 4, 913
Aiello, S., Akrame, S. E., Ameli, F., et al. 2019, APh, 111, 100
Aramaki, T., Adrian, P. O. H., Karagiorgi, G., & Odaka, H. 2020, APh, 114, 107
Avrorin, A. D., Avrorin, A. V., Aynutdinov, V. M., et al. 2014, NIMPA, 742, 82
Becker, J. K. 2008, PhR, 458, 173
Beloborodov, A. M. 2003, ApJ, 588, 931
Berger, E. 2014, ARA&A, 52, 43
Blandford, R., & Eichler, D. 1987, PhR, 154, 1
Bromberg, O., Nakar, E., Piran, T., & Sari, R. 2011, ApJ, 740, 100
Caputo, R., Ajello, M., Kierans, C., et al. 2022, JATIS, 8, 044003
Chodorowski, M. J., Zdziarski, A. A., & Sikora, M. 1992, ApJ, 400, 181
Coward, D. M., Howell, E. J., Piran, T., et al. 2012, MNRAS, 425, 2668
Dai, Z. G., & Lu, T. 1998, A&A, 333, L87
De Angelis, A., Tatischeff, V., Tavani, M., et al. 2017, ExA, 44, 25
Dermer, C. D., Murase, K., & Takami, H. 2012, ApJ, 755, 147
Ghirlanda, G., Salafia, O. S., Paragi, Z., et al. 2019, Sci, 363, 968
Gompertz, B. P., O'Brien, P. T., & Wynn, G. A. 2014, MNRAS, 438, 240
Guetta, D., Hooper, D., Alvarez-Muniz, J., Halzen, F., & Reuveni, E. 2004, APh, 20, 429
Guo, F., Liu, Y.-H., Li, X., et al. 2020, PhPl, 27, 080501
Hamidani, H., & Ioka, K. 2021, MNRAS, 500, 627
Hamidani, H., & Ioka, K. 2023, MNRAS, 520, 1111
Hamidani, H., Kiuchi, K., & Ioka, K. 2020, MNRAS, 491, 3192
He, H.-N., Liu, R.-Y., Wang, X.-Y., et al. 2012, ApJ, 752, 29
Hümmer, S., Baerwald, P., & Winter, W. 2012, PhRvL, 108, 231101
IceCube Collaboration, Abbasi, R., Ackermann, M., et al. 2021, arXiv:2101.09836
IceCube Collaboration, Abbasi, R., Abdou, Y., et al. 2012, Natur, 484, 351
Ioka, K., Kobayashi, S., & Zhang, B. 2005, ApJ, 631, 429
Kagawa, Y., Yonetoku, D., Sawano, T., et al. 2015, ApJ, 811, 4
Kagawa, Y., Yonetoku, D., Sawano, T., et al. 2019, ApJ, 877, 147
Kaneko, Y., Bostancı, Z. F., Göğüş, E., & Lin, L. 2015, MNRAS, 452, 824
Kasen, D., Metzger, B., Barnes, J., Quataert, E., & Ramirez-Ruiz, E. 2017, Natur, 551, 80

Kasliwal, M. M., Nakar, E., Singer, L. P., et al. 2017, Sci, 358, 1559
Kimura, S. S. 2022, arXiv:2202.06480
Kimura, S. S., Murase, K., Bartos, I., et al. 2018, PhRvD, 98, 043020
Kimura, S. S., Murase, K., Ioka, K., et al. 2019, ApJL, 887, L16
Kimura, S. S., Murase, K., Mészáros, P., & Kiuchi, K. 2017, ApJL, 848, L4
Kisaka, S., & Ioka, K. 2015, ApJL, 804, L16
Kisaka, S., Ioka, K., & Sakamoto, T. 2017, ApJ, 846, 142
Kohri, K., Narayan, R., & Piran, T. 2005, ApJ, 629, 341
Lamb, G. P., Lyman, J. D., Levan, A. J., et al. 2019, ApJL, 870, L15
Levinson, A., & Eichler, D. 2003, ApJL, 594, L19
Li, Z. 2012, PhRvD, 85, 027301
Matsumoto, T., & Kimura, S. S. 2018, ApJL, 866, L16
Mei, A., Banerjee, B., Oganesyan, G., et al. 2022, Natur, 612, 236
Metzger, B. D., Quataert, E., & Thompson, T. A. 2008, MNRAS, 385, 1455
Moharana, R., & Piran, T. 2017, MNRAS, 472, L55
Mooley, K. P., Frail, D. A., Dobie, D., et al. 2018a, ApJL, 868, L11
Mooley, K. P., Nakar, E., Hotokezaka, K., et al. 2018b, Natur, 554, 207
Murase, K., & Ioka, K. 2013, PhRvL, 111, 121102
Murase, K., & Nagataki, S. 2006a, PhRvD, 73, 063002
Murase, K., & Nagataki, S. 2006b, PhRvL, 97, 051101
Murguia-Berthier, A., Ramirez-Ruiz, E., Kilpatrick, C. D., et al. 2017, ApJL, 848, L34
Norris, J. P., & Bonnell, J. T. 2006, ApJ, 643, 266
Perna, R., Armitage, P. J., & Zhang, B. 2006, ApJL, 636, L29
Rastinejad, J. C., Gompertz, B. P., Levan, A. J., et al. 2022, Natur, 612, 223
Rees, M. J., & Mészáros, P. 2005, ApJ, 628, 847
Rouco Escorial, A., Fong, W.-F., Berger, E., et al. 2022, arXiv:2210.05695
Rowlinson, A., O'Brien, P. T., Metzger, B. D., Tanvir, N. R., & Levan, A. J. 2013, MNRAS, 430, 1061
Sakamoto, T., Barthelmy, S. D., Baumgartner, W. H., et al. 2011, ApJS, 195, 2
Sarin, N., Lasky, P. D., Vivanco, F. H., et al. 2022, PhRvD, 105, 083004
Shibata, M., Fujibayashi, S., Hotokezaka, K., et al. 2017, PhRvD, 96, 123012
Stepney, S., & Guilbert, P. W. 1983, MNRAS, 204, 1269
Tanaka, M., Utsumi, Y., Mazzali, P. A., et al. 2017, PASJ, 69, 102
Toma, K., Wu, X.-F., & Mészáros, P. 2009, ApJ, 707, 1404
Troja, E., Fryer, C. L., O'Connor, B., et al. 2022, Natur, 612, 228
Troja, E., Piro, L., Ryan, G., et al. 2018, MNRAS, 478, L18
Wanderman, D., & Piran, T. 2015, MNRAS, 448, 3026
Waxman, E., & Bahcall, J. 1997, PhRvL, 78, 2292
Waxman, E., & Bahcall, J. 1998, PhRvD, 59, 023002
Xue, Y. Q., Zheng, X. C., Li, Y., et al. 2019, Natur, 568, 198
Yang, J., Ai, S., Zhang, B.-B., et al. 2022, Natur, 612, 232
Ye, Z. P., Hu, F., Tian, W., et al. 2022, arXiv:2207.04519
Zhang, B., & Kumar, P. 2013, PhRvL, 110, 121101
Zhang, B., & Yan, H. 2011, ApJ, 726, 90
Zhang, H.-M., Huang, Y.-Y., Zheng, J.-H., Liu, R.-Y., & Wang, X.-Y. 2022, ApJL, 933, L22